An L-band model function for the ocean-normalized radar cross section derived from PALSAR

Osamu Isoguchi(1) **and Masanobu Shimada**(1)

(1) Earth Observation Research Center, Japan Aerospace Exploration Agency
2-1-1 Sengen, Tsukuba, Ibaraki, 305-8505, Japan
E-mail:isoguchi.osamu@jaxa.jp

Abstract
The relationship between ocean wind vectors and L-band normalized radar cross sections (NRCS) is comprehensively examined to propose an L-band model function by using the Phased-Array L-band Synthetic Aperture Radar (PALSAR) and scatterometer wind data. Based on more than 90,000 match-ups, the L-band NRCS dependence on wind speed, incidence angle, and relative wind direction is modeled for the 0-20 m/s wind speed and 17-43º incidence angle ranges. Wind speeds are then inversely estimated from the mutch-ups and compared with the reference winds, resulting in the -0.16 m/s bias and 2.31 m/s root mean square (rms) error. Crosswind data show poor estimation, probably due to the NRCS-wind relation temporarily saturated around 10 m/s.

Keywords: PALSAR, L-band model function, wind speed retrieval

1. INTRODUCTION

Synthetic Aperture Radar (SAR) can provide high-spatial-resolution images of ocean-surface roughness. It can be used to estimate wind speed even in coastal areas. Wind stress variations on the sea surface modulate the roughness, changing the backscattered radar power, usually expressed as normalized radar cross sections (NRCS). An empirical relation between NRCS and wind speeds known as the geophysical model function (GMF) has been established originally for scatterometers [1] [2] [3]. The C-band model functions have recently been applied for the ERS-1/2, ENVISAT, and RADARSAT SAR images to detect high-resolution wind fields.
Along with the C-band SAR, the several space-borne L-band SAR were operated, providing the L-band NRCS images. By using these SAR-derived NRCS, the L-band NRCS dependence on wind fields has been investigated [4], [5]. However, these relations are rough and/or are applied to limited cases because of data limitation. In January 2006, the Japan Aerospace Exploration Agency (JAXA) launched the Advanced Land Observing Satellite (ALOS), which carries the Phased-Array L-band Synthetic Aperture Radar (PALSAR). PALSAR can observe the Earth with various off-nadir angles and has a ScanSAR function that enabled us to investigate the L-band NRCS dependence extensively. In this study, we investigate the relationship between NRCS from PALSAR and co-located wind data and propose an L-band model function applied for PALSAR.

2. DATA

2.1. L-band HH NRCS

In order to collect the L-band HH NRCS, we use PALSAR data observed with the ScanSAR HH mode from 24 March, 2007 to 31 July, 2007. The strip slant-range covers a 350km swath with incidence angles ranging from 17º to 43º. The digital numbers (DN) of the 16-bit PALSAR images are converted to the NRCS by applying a calibration factor as,

$$\sigma^o = 10 \cdot \log_{10} \left\langle DN^2 \right\rangle + CF \quad , \qquad (1)$$

where CF is a calibration factor which is defined as a constant value of -83 dB. The radiometric accuracy is critical for wind speed retrieval by SAR. During the ALOS initial calibration phase, the radiometric accuracy of PALSAR was reported to be 0.64 dB (1σ) by using in-total 500 calibration points collected worldwide.

2.2. ASCAT wind data

For reference wind data, we use the Advanced Scatterometer (ASCAT) 25-km demonstration wind product, which are provided by the Royal Netherlands Meteorological Institute (KNMI). The ASCAT onboard the MetOp satellite is a C-band scatterometer, which estimates wind speed and directions based on the CMOD5 [3]. The orbit configuration of the MetOp satellite is relatively close to that of ALOS. This orbit configuration enables us to collect match-ups with relatively small observational time gaps between the PALSAR NRCS and ASCAT ocean winds.
The data we use are the global wind speeds and directions with a 25×25 km grid. An initial calibration conducted by a comparison with about the 300,000 European Center for Medium range Weather Forecasting (ECMWF) ocean winds showed good data quality: the bias and root mean square (RMS) error of wind speed are -0.02 m/s and 1.26 m/s and those of wind direction are 0.86° and 15.01°.

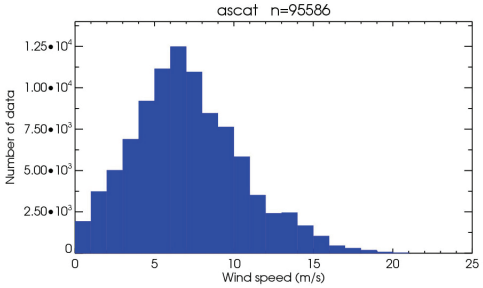

Figure 1. Histogram of the match-ups with respect to wind speed.

2.3. Match-up data

Match-up data, which consist of the L-band HH NRCS, incidence angles, wind speeds, and relative wind directions are collected from the PALSAR images and the co-located ASCAT wind vectors. The relative wind direction represents the difference between the wind direction and the PALSAR beam angle, where upwind is defined as zero. We collected the match-ups in the case when the observational gap is less than 90 minutes. The NRCS are calculated for a region of about 5×5 km centered at the wind observation points.

In order to investigate the dependency of NRCS on wind speed, wind direction, and incidence angle, the match-ups are classified into "bins" of the 1m/s wind speed, the 11.25º wind direction, and the 5.2º incidence angle. Any data whose deviation exceeds 3σ in each bin is excluded. In total, 95,586 match-ups are collected. Fig. 1 shows a histogram with respect to the wind speed. The match-ups in the wind range stronger than 15 m/s is limited. Thus the result derived in this study is relatively reliable for the wind speed range below 15 m/s.

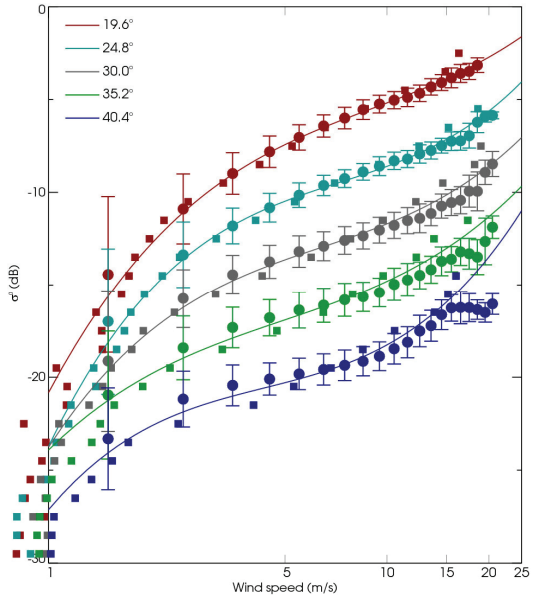

Figure 2. A_0 plots as a function of logarithm of wind speed, on which the derived A_0 function is superimposed.

3. RESULTS

The GMF of NRCS over the ocean is generally expressed as,

$$\sigma^o = A_0(v,\theta)(1+A_1(v,\theta)\cos\varphi+A_2(v,\theta)\cos 2\varphi), \quad (2)$$

where σ^o is the NRCS, v is the wind speed, θ is the incidence angle, φ is the wind direction and A_n (v,θ) (i=0,1,2) are functions of the wind speed and incidence angle.

The A_n (v,θ) (i=0,1,2) are calculated by the following sequence of processes. 1) The approximation formula of A_0 is modeled to fit the binned averages of NRCS with respect to the wind speed and incidence angle. 2) Based on the derived A_0, the following Fourier term is calculated for each match-up as,

$$\frac{\sigma^o}{A_0} - 1 = A_1 \cos\varphi + A_2 \cos 2\varphi\,, \quad (4)$$

and is plotted as a function of wind direction for each wind speed and incidence angle bin. The A_1 and A_2 are then calculated for each bin by the least square fitting and are modeled as functions of the wind speed and incidence angle. 3) The above 1) and 2) processes are iterated until they converse well enough to determine the final A_n (i=0,1,2) model functions. In the second or later A_0 derivation process, the σ^o is first modified to take wind direction dependency into account based on the derived A_1 and A_2 formula as,

$$\sigma^{o\prime} = \frac{\sigma^o}{1 + A_1 \cos\varphi + A_2 \cos 2\varphi}, \quad (5)$$

where $\sigma^{o\prime}$ is modified NRCS. In the actual process, solutions almost converge with one iteration and the final results are shown in the following sections.

3.1. A_0 relation

Fig. 2 depicts the A_0 plots with respect to the logarithm of wind speed for each incidence angle bin, on which the final approximation formula of A_0 are superimposed. Although the A_0 gradually increases with the wind speed, it is not a simple power law relation: the A_0 increasing rates, being relatively gentle at moderate winds (4-12 m/s), become large especially at stringer winds (> 12 m/s). In this study, the A_0 is approximated as a cubic function of the logarithm of wind speed as Eq. A1 (in Appendix), in which respective coefficients (a0-a4) are expressed as a quadratic function of θ as Eqs. A2. Because the number of the match-ups is limited at strong winds (>20 m/s) where the C-band NRCS saturates, the relation at these ranges are not involved in the current model function. The behavior of the L-band NRCS at strong winds is one of interesting targets in the future study.

3.2. Wind direction dependency

Fig. 3 represents the A_1 and A_2 plots with respect to wind speed for each incidence angle bin. The upwind-downwind amplitude (A_1) of the high incidence angle (θ=40.4º) increases with the increase of wind speed, whereas that of the low incidence angle (θ=19.6º) decreases, changing its sign around 8 m/s. As a result, the upwind-downwind amplitudes show opposite tendency at strong winds, depending on incidence angles: the upwind NRCS is larger (smaller) than the downwind at large (small) incidence angles. The A_1 is modeled as a polynomial function of v and θ as Eq. A3. The approximation formulas at each incidence angle are superimposed on Fig. 3(a).

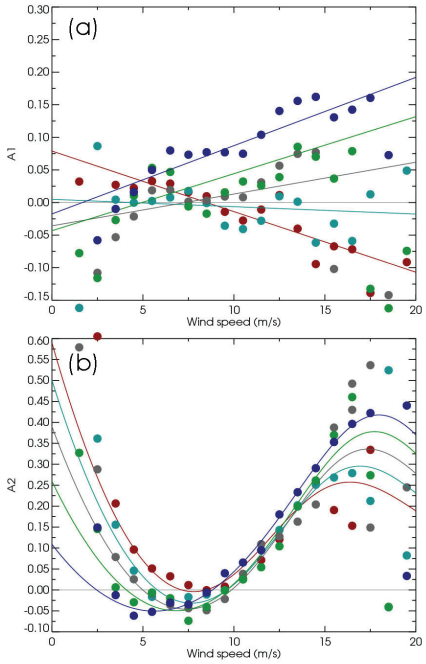

Figure 3. A_1 and A_2 plots as a function of wind speed, on which the derived functions are superimposed.

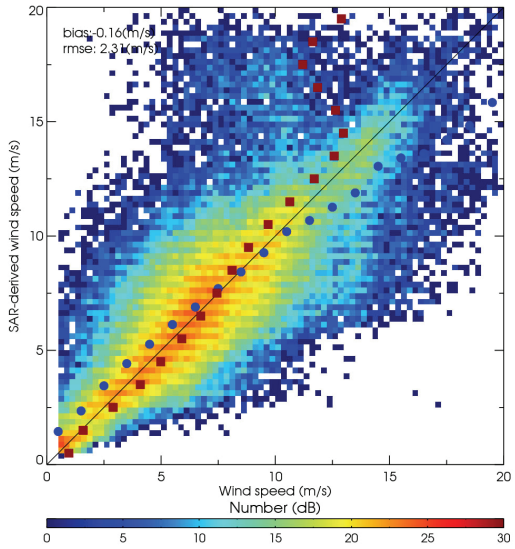

Figure 4. Scatter plot between ASCAT and PALSAR-derived winds.

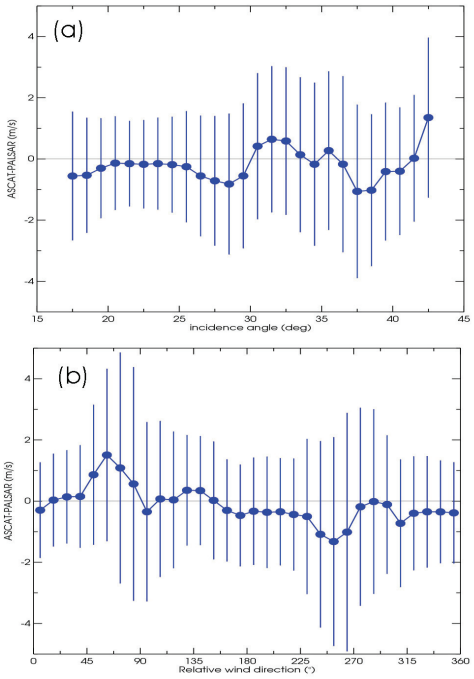

Figure 5. Errors (ASCAT-PALSAR) as functions of (a) wind speed and (b) wind direction.

The upwind-crosswind amplitude (A_2) represents a horseshoe shape with saturation at strong winds, where those at moderate winds (4-10 m/s) are almost zero (Fig. 3(b)). The saturations at string winds are not so reliable yet due to the limited number of the match-ups. Upward tendency with the decrease of wind speeds < 5 m/s is remarkable. The same upward change has been reported from airborne measurements operated with C-band and Ku-band [6]. They pointed out that crosswind NRCS declines rapidly at low winds due to viscous damping. Although the C-band NRCS derived from the ERS-2 scatterometer has represented the similar pattern, it was not involved in the model function (CMOD5) [3].

In order to model the A_2, we apply Eq. A4, which combines a quadratic function of wind speed with the saturation at strong winds. Respective coefficients are expressed as linear functions of θ as Eqs. A5. It should be noted that because the derived A_2 at strong winds (> 15 m/s) are unreliable due to the limited data number, the model function is determined for the A_2 values modified to be constant at strong winds > 15 m/s. The derived model function is superimposed in Fig. 3(b).

3.3. Wind fit

Wind speeds are inversely estimated from the match-up data by applying the derived model function. They are then compared with the ASCAT reference wind speeds. Fig. 4 shows their scatter plots, where colors indicate data number within bin (in dB), circles and squares represent binned averages with respect to the ASCAT and PALSAR-derived winds, respectively. The bias and root mean square

(rms) error of differences (ASCAT-PALSAR) are -0.16 m/s and 0.31 m/s.

Here we look at error tendency. Fig. 5 depicts the error (the bias and rms error) as functions of incidence angles and relative wind directions. The rms error increases with incidence angle increasing: the 1.2 m/s rms error at 20-25º incidence angles rises by a factor of 2 at 35-40º. This is probably attributed to 1) the larger noise level of the NRCS and 2) the smaller increasing rates of A_0 at high incidence angles. The former gives rise to the large variance of the NRCS, which is shown as the vertical bars in Fig. 2. The large variance leads to the large rms error of the estimated wind speed. As for the latter factor, as shown in Fig. 2, the increasing rates with respect to wind speed decrease with the increasing of incidence angle. With the same radiometric accuracy of the NRCS, the small increasing rate (gentle slope) results in poor wind estimations. The error dependence on wind direction (Fig. 5(b)) indicates that while the relatively good estimation (1.8 m/s rms error) is achieved for the upwind and downwind data, the crosswind data generate the large rms error of about 3 m/s. This is likely to be caused by the fact that the crosswind NRCS at large incidence angles temporarily saturate with respect to wind speed around 10 m/s wind ranges. This saturation effect is expressed as large deviations scattering around 10 m/s in Fig. 4.

4. CONCLUDING REMARKS

We investigated comprehensively the L-band HH NRCS dependence on wind fields and proposed the L-band HH GFM. Although the study showed the promising result, there still remain some matters that we have to consider. The current function was developed to fit the PALSAR-derived L-band NRCS. Because the SAR-derived NRCS are generally affected by the larger noise level at large incidence angles, these noise effects on the function should be evaluated especially at large incidence angles. As mentioned above, the L-band NRCS response at strong winds (> 20 m/s), where the C-band saturates, is one of the interesting targets. By accumulating more match-ups, it will be answered in the future study.

Appendix

The A_0 term of Eq. 2 is defined as,

$$A_0 = 10^{(a_0 + a_1 W + a_2 W^2 + a_3 W^3)/10}, \quad \text{(A1)}$$

where $W=10\log_{10}v$. The functions a_0, a_1, a_2, and a_3 depend on incidence angle:

$$a_0 = c_1 + c_2 x + c_3 x^2$$
$$a_1 = c_4 + c_5 x + c_6 x^2$$
$$a_2 = c_7 + c_8 x + c_9 x^2$$
$$a_3 = c_{10} + c_{11} x + c_{12} x^2, \quad \text{(A2)}$$

where $x=(\theta-30)/15$. The c_n coefficients are listed in Tab. A1.

The A_1 term of Eq. 2 is defined as,

$$A_1 = c_{13} + c_{14} x + c_{15} x^2 + (c_{16} + c_{17} x + c_{18} x^2) v. \quad \text{(A3)}$$

The B2 term is modeled as follows:

$$A_2 = \frac{b_0 + b_1 v + b_2 v^2}{1 + \exp(b_3 + b_4 v)}. \quad \text{(A4)}$$

The functions b_0, b_1, b_2, and b_3 depend on incidence angle:

$$b_0 = c_{19} + c_{20} x$$
$$b_1 = c_{21} + c_{22} x$$
$$b_2 = c_{23} + c_{24} x$$
$$b_3 = c_{25} + c_{26} x$$
$$b_4 = c_{27} + c_{28} x. \quad \text{(A5)}$$

This formula can be applied for the following wind speed and incidence angle ranges: $v < 20$ m/s, $17º < \theta < 43º$.

Table 1. Coefficients of the model function

c_1	-22.4616	c_{15}	0.15687361
c_2	-4.63708	c_{16}	0.0043790155
c_3	-3.34334	c_{17}	0.013130485
c_4	2.22557	c_{18}	-0.012174920
c_5	-0.868219	c_{19}	0.58472518
c_6	1.29422	c_{20}	-0.31193716
c_7	-0.196280	c_{21}	-0.17318385
c_8	0.0112295	c_{22}	0.057750363
c_9	-0.185301	c_{23}	0.011936887
c_{10}	0.00817458	c_{24}	-0.0027975424
c_{11}	0.00278560	c_{25}	-3.0464364
c_{12}	0.00861381	c_{26}	-0.72583002
c_{13}	-0.028709343	c_{27}	0.23126559
c_{14}	-0.06620837	c_{28}	0.00016379017

References

[1] A. Stoffelen, and D. Anderson, "Scatterometer data interpretation: Estimation and validation of the transfer function CMOD4", J. Geophys. Res., vol. 102, pp.5767-5780, 1997.

[2] F. J. Wentz, and D. K. Smith, "A model function for the ocean-normalized radar cross section at 14 GHz derived from NSCAT observations", J. Geophys. Res., vol. 104, pp.11499-11514, 1999.

[3] H. Hersbach, A. Stoffelen, and S. de Haan, "An improved C-band scatterometer ocean geophysical model function: CMOD5", J. Geophys. Res., vol. 112, doi:10.1029/2006JC003743, 2007.

[4] T. W. Thompson, D. E. Weissman, and F. I. Gonzalez, "L band radar backscatter dependence upon surface wind stress: A summary of new SEASAT-1 and Aircraft observations", J. Geophys. Res., vol. 88, pp. 1727-1735, 1983.

[5] T. Shimada, H. Kawamura, M. Shimada, "An L-band geophysical model function for SAR wind retrieval using JERS-1 SAR", IEEE Trans. Geosci. Remote Sensing, vol. 41, pp.518-531, 2003.

[6] J. R. Carswell, W. J. Donnelly, R. E. McIntosh, M. A. Donelan, and D. C. Vandemark, "Analysis of C and Ku band ocean backscatter measurements under low-wind conditions", J. Geophys. Res., vol. 104, 20,678-20,701, 1999.